Letter

Quantum-well tunneling anisotropic magnetoresistance above room temperature

Muftah Al-Mahdawi,[1,2,3,*,†] Qingyi Xiang,[1,*] Yoshio Miura,[1,4,*,‡] Mohamed Belmoubarik,[1] Keisuke Masuda,[1] Shinya Kasai,[1] Hiroaki Sukegawa,[1] and Seiji Mitani[1,5,§]

[1]*National Institute for Materials Science, Tsukuba 305-0047, Japan*

[2]*Center for Science and Innovation in Spintronics (Core Research Cluster), Tohoku University, Sendai 980-8577, Japan*

[3]*Center for Spintronics Research Network, Tohoku University, Sendai 980-8577, Japan*

[4]*Center for Spintronics Research Network, Osaka University, Toyonaka 560-8531, Japan*

[5]*Graduate School of Pure and Applied Sciences, University of Tsukuba, Tsukuba 305-0047, Japan*

(Received 3 July 2019; revised 1 April 2021; accepted 10 May 2021; published 25 May 2021)

Quantum-well (QW) devices have been extensively investigated in semiconductor structures. More recently, spin-polarized QWs were integrated into magnetic tunnel junctions (MTJs). In this Letter, we demonstrate the spin-based control of the quantized states in iron 3*d*-band QWs, as observed in experiments and theoretical calculations. We find that the magnetization rotation in the Fe QWs significantly shifts the QW quantization levels, which modulate the resonant-tunneling current in MTJs, resulting in a tunneling anisotropic magnetoresistance (TAMR) effect of QWs. This QW-TAMR effect is sizable compared with other types of TAMR effect, and it is present above room temperature. In a QW MTJ of Cr/Fe/$MgAl_2O_4$/top electrode, where the QW is formed by a mismatch between Cr and Fe in the *d* band with Δ_1 symmetry, a QW-TAMR ratio of up to 5.4% was observed at 5 K, which persisted to 1.2% even at 380 K. The magnetic control of QW transport can open new applications for spin-coupled optoelectronic devices, ultrathin sensors, and memory.

DOI: 10.1103/PhysRevB.103.L180408

Quantum-well (QW) devices have found wide adoption in semiconductor technologies, such as QW-based lasers and high-mobility transistors [1,2]. On the other hand, metallic QWs can incorporate the large exchange splitting on *d* electrons in spin-polarized QW devices [3–7]. In more recent technological advances, spin-polarized *d*-band QWs were demonstrated in magnetic tunnel junctions (MTJs), where the confinement potential is produced both by band-gap and band-symmetry mismatches [8–11].

MTJs have been the prominent driver in spintronics research and applications. Especially, the Fe alloys/MgO MTJs possess a giant tunneling magnetoresistance (TMR) effect [12,13], due to the symmetry-selective filtering of *d* states [14]. Another different effect is the anisotropic change of tunneling resistance of MTJs with the relative angle between tunneling current and magnetization direction. This tunneling anisotropic magnetoresistance (TAMR) effect stems from the changes in the density of states near the Fermi level, due to spin-orbit coupling (SOC) effects [15–23]. The TAMR effect has been of interest for understanding the important role of SOC at ferromagnetic (FM) interfaces and for applications requiring ultrathin spintronic sensors and memory, because of the need for only a single FM electrode. The TAMR effect has been reported for large-SOC materials, such as GaMnAs [15,24], Co/Pt [20], and IrMn [21]. In single-crystal Fe/MgO MTJs, the TAMR effect was observed [22], and it was related to the combined effect of SOC and the asymmetric crystal field at the interface [22,25].

In this Letter, we find a TAMR effect linked to the transport through QW resonant states (QWRSs) in a ferromagnetic QW structure. The narrow QWRSs couple to the magnetization direction through SOC, and the magnetization rotation controls the energy positions and broadening of QWRSs. Therefore the magnetization anisotropically controls the resonant tunneling condition, and a sizable QW-TAMR effect is obtained [Fig. 1(a)]. This QW-TAMR effect is qualitatively different from the much smaller TAMR effect in MTJs with bulk electrodes. Furthermore, the QW-TAMR effect is sustained above room temperature, compared with other TAMR effects, which were observed only at cryogenic temperatures.

In the QW structure of Cr/Fe/oxide, the resonant tunneling is through QWRSs that form for the majority-spin electronic states of Δ_1 symmetry ($\Delta_{1,\uparrow}$), due to a mismatch of Δ_1 bands of Fe and Cr [9,26]. In contrast to the rocksalt-type MgO, the spinel $MgAl_2O_4$ has a small lattice mismatch of $< 1\%$ with Fe. A dislocation-free Fe/$MgAl_2O_4$ interface can be realized [27,28], which significantly enhances the phase coherence in QW structures [10,11]. We measure the QW-TAMR effect in epitaxial stacks of Cr/Fe/$MgAl_2O_4$, with the geometry and coordinates depicted in Fig. 1(b). The detailed film stack is MgO (001) substrate/MgO (5)/Cr (40)/Fe (t_{Fe})/$MgAl_2O_4$ (2)/Fe (0.5)/$Co_{60}Fe_{20}B_{20}$(CoFeB) (5)/Ru (10) (thicknesses in nanometers), where $t_{Fe} = 0.70$ and 0.84 nm correspond to five and six monolayers (MLs), respectively. We used electron-beam evaporation and magnetron sputtering to prepare the epitaxial MTJ films. Postannealing

*These authors contributed equally to this work.
†mahdawi@mlab.apph.tohoku.ac.jp
‡miura.yoshio@nims.go.jp
§mitani.seiji@nims.go.jp.

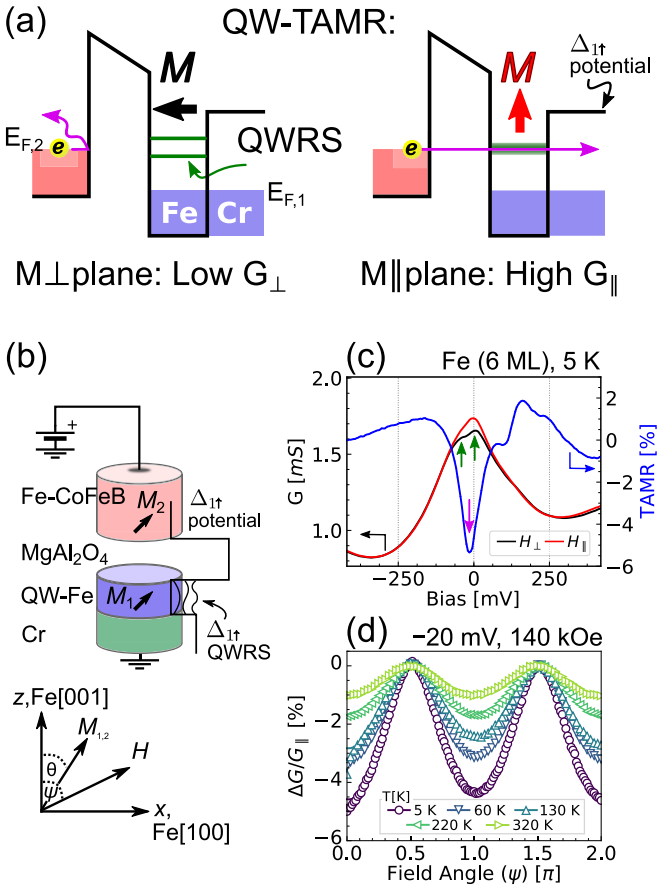

FIG. 1. The QW-TAMR effect. (a) In an Fe QW, the M rotation shifts and broadens the sharp QW states, resulting in a large anisotropy of tunneling resistance (TAMR). (b) A schematic of the QW stack, and the definitions of coordinates. (c) The fine features of resonant conduction (green arrows) are anisotropic with respect to the M direction, resulting in a large QW-TAMR ratio (magenta arrow). (d) The QW-TAMR effect is twofold symmetric and persists above 300 K.

after each deposition step was done *in situ* to improve crystallinity and flatness, except for the top Fe/CoFeB layer, which was left as deposited. Therefore the top electrode provides an isotropic electrode for $\Delta_{1,\uparrow}$ electrons, due to the lack of crystallinity and the small TAMR in CoFeB [17]. Structural analysis showed a lattice-matched (001)-oriented epitaxial layer-by-layer growth and flat $MgAl_2O_4$ interfaces [29,30]. The films were microfabricated into elliptical junctions with a cross section of 5×2.5 μm, where the major axis was along the Fe [100] axis. Further details on the preparation and TMR properties are provided in Ref. [11]. As a comparison sample, we use a high-TMR non-QW sample epitaxially grown by sputtering with thick Fe electrodes [28], with the film stack of MgO (001) substrate/Cr (40)/Fe (100)/$MgAl_2O_4$ (2.17)/Fe (7)/IrMn (12)/Ru (10) (thicknesses in nanometers), which has a TMR ratio of 401% at 5 K and 224% at 300 K.

We applied large saturating magnetic fields, and at each applied field angle ψ we measured the I-V curves at 1- to 5-mV steps with the four-wire method in a physical property measurement system, using source meters and nanovoltmeters.

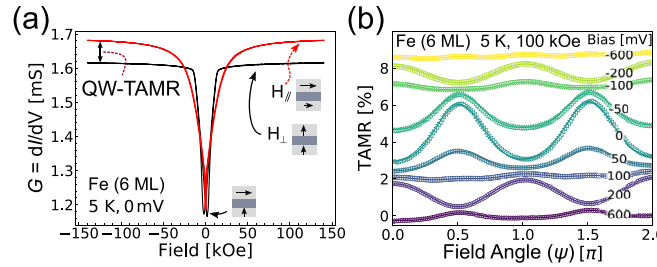

FIG. 2. Distinguishing QW-TAMR from TMR. (a) The G-H curves show a large QW-TAMR effect between the in-plane and perpendicular fields above saturation. (b) The angular dependence of TAMR shows a strong dependence on bias. The solid lines are fitting curves to Eq. (1), and there is a vertical shift for clarity.

Subsequently, we numerically calculated the differential tunneling conductance $G = dI/dV$. The positive bias is defined as electrons tunneling towards the top electrode.

At a Fe-QW thickness of six MLs, a QWRS forms near the Fermi level, as seen by the peak near zero bias in the G spectra [Fig. 1(c)]. The single G resonance peak splits into two fine-structure peaks, when the magnetization M is rotated by a saturating magnetic field ($H = 140$ kOe) from the in-plane to out-of-plane direction [the green arrows in Fig. 1(c)]. This split is the main origin of the QW-TAMR effect, which has a maximum magnitude in between the fine-structure peaks [the magenta arrow in Fig. 1(c)]. The symmetry of the QW-TAMR effect is twofold with regard to the out-of-plane field rotation angle [Fig. 1(d)]. Furthermore, the QW-TAMR effect decreases gradually with increasing temperature and is still present above the room temperature [Fig. 1(d)]. We should note that there is a small fourfold component. This fourfold component is from the small misalignment of magnetization and field, and not intrinsic in origin [31], as discussed in the Supplemental Material [32]. Above the saturation field, there is no significant effect of H magnitude (Sec. S1 in the Supplemental Material [32]). Moreover, the QW-TAMR spectra are equivalent for M rotations in either Fe (100) or Fe (110) planes. The in-plane (001) rotation has a zero QW-TAMR (Sec. S2 in the Supplemental Material [32]). Therefore the out-of-plane asymmetry is the main component of the QWRS modulation.

In Figs. 2 and 3, we show the distinction of the QW-TAMR effect from the commonly observed TMR and TAMR effects. The G-H curves in the in-plane ($H_\parallel$) or out-of-plane ($H_\perp$) applied magnetic field directions are shown in Fig. 2(a). The low conductance at zero field is due to the TMR effect and is not of concern in this Letter. It is due to the nonparallel orthogonal magnetic configuration formed by the large perpendicular magnetic anisotropy at the bottom Fe/$MgAl_2O_4$ interface [30]. On the other hand, the top and bottom electrodes' magnetization vectors $M_{1,2}$ are parallel at a high field above saturation ($|H| > 50$ kOe). The conductances G in the $H_\parallel$ and $H_\perp$ field directions are not equal [Fig. 2(a)], resulting in an anisotropic tunneling conductance. This is what distinguishes TAMR, where conductance depends on the absolute angle θ of M, from the usual TMR effect, where conductance depends on relative angle between two magnetizations.

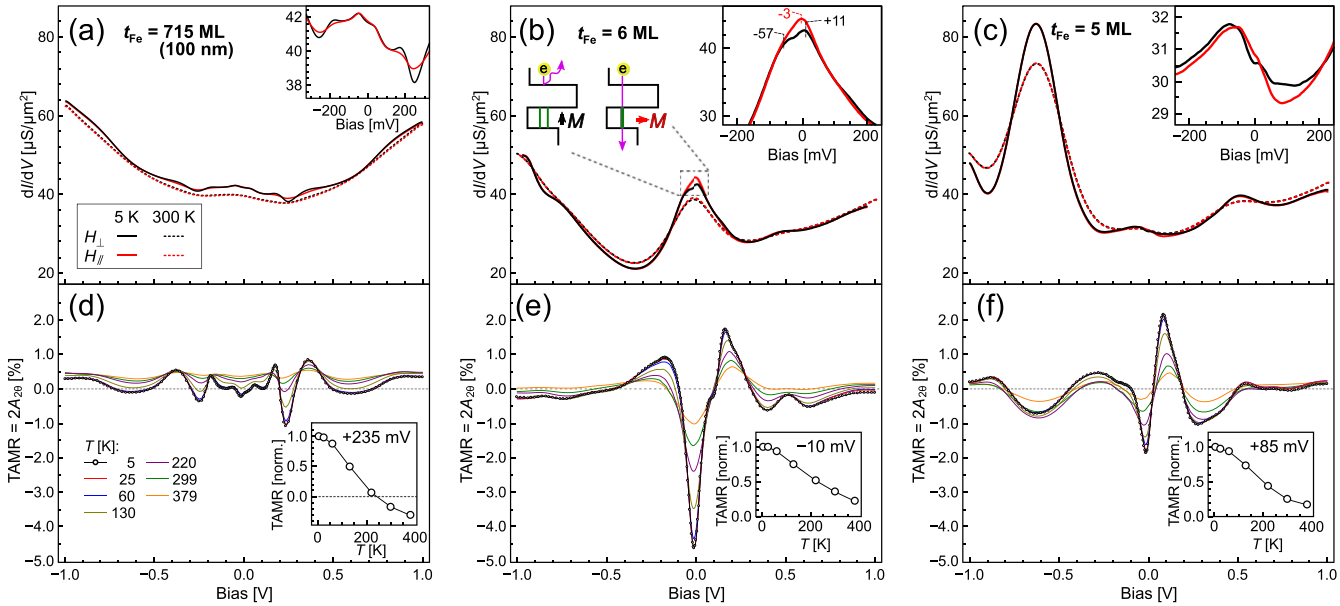

FIG. 3. The effect of QW formation on G and TAMR spectra. (a)–(c) G spectra at 5 K (solid lines) and 300 K (dashed lines). Black and red lines were obtained at saturating $H_\perp$ and $H_\parallel$, respectively. The insets are enlarged views near zero bias. The thickness of Fe t_{Fe} is indicated on the plots. (d)–(f) The temperature dependence of TAMR spectra. The insets in (d)–(f) show the temperature dependence of the largest TAMR peak normalized to its 5-K value.

Furthermore, the twofold nature of the QW-TAMR effect is shown by the dominant twofold symmetry of the dependence of G on field angle ψ, above the saturation field at $H = 100$ kOe [Fig. 2(b)]. As the voltage bias is increased away from the QWRS near zero bias, the QW-TAMR shows a strong modulation in sign and magnitude, but the twofold symmetry is preserved. We extract QW-TAMR spectra from fits to the ψ dependence of G at each bias, using the following definition of TAMR ratio:

$$\mathrm{TAMR}(\psi) = \frac{G(\psi)}{G(90^\circ)} - 1 \tag{1a}$$

$$= \mathrm{const} + a_{2\psi}\cos 2\psi + a_{4\psi}\cos 4\psi \tag{1b}$$

$$\equiv \mathrm{const} + A_{2\theta}\cos 2\theta, \tag{1c}$$

where $a_{2\psi}$ is the QW-TAMR apparent twofold component in ψ and $a_{4\psi}$ is the corresponding fourfold component. QW-TAMR shows only an intrinsic twofold symmetry $A_{2\theta}$ in the magnetization angle θ, which is linked to $a_{2\psi}$ and $a_{4\psi}$ as follows (Sec. S1 in the Supplemental Material [32]):

$$A_{2\theta} \approx a_{2\psi} - 2a_{4\psi}. \tag{2}$$

Figure 3 shows the distinction between the QW-TAMR and TAMR of bulk electrodes, the effect of QWRS position, and temperature dependence. We show the three cases of a bulk-electrode sample ($t_{Fe} = 715$ MLs $= 100$ nm) and two QWs ($t_{Fe} = 6$ and 5 MLs). Figures 3(a)–3(c) show the G-V spectra in the $H_\parallel$ and $H_\perp$ field directions. Figures 3(d)–3(f) show the $A_{2\theta}$-V spectra extracted from Eq. (2), including the temperature dependence.

In contrast to the non-QW sample in Fig. 3(a), the QW-Fe samples have the resonant tunneling peaks through the QWRS near 0 V for $t_{Fe} = 6$ MLs and at -0.6 V for $t_{Fe} = 5$ MLs [Figs. 3(b) and 3(c)]. The QW resonance peaks in G-V curves are sustained at room temperature and above [the dashed lines in Figs. 3(b) and 3(c)]. The presence of the QWRS at high temperatures is due to the phase coherence in $Cr/Fe/MgAl_2O_4$ QWs. The peak broadening of QWRS peaks by the carrier finite lifetime [33,34] ranges from 0.23 to 0.40 eV. We estimate the maximum bound on the majority carrier lifetime at 2.8×10^{-15} s and that the mean free path is 3.3 nm, which are close to reported values on majority spin carriers in Fe [9,35]. The ultrathin QW produces a large separation between QWRSs, on the order of 0.5–1.0 eV, which is much larger than the QWRS broadening by the thermal energy or carrier lifetime. On the other hand, the non-QW sample shows a smoothing of G-V curve features by increasing the temperature [Fig. 3(a)].

The QW formation and thickness cause a drastic change to TAMR spectra, as seen in Figs. 3(d)–3(f). Also, relatively large QW-TAMR magnitudes are observed at our maximum measurement temperature of 380 K [Figs. 3(e) and 3(f) and the insets therein]. In the non-QW sample, G-V and TAMR-V spectra have shallow valleys at ± 0.25 V [Fig. 3(a)]. The TAMR and G spectra in thick-$Fe/MgAl_2O_4$ are qualitatively similar to the MgO barrier [22,36] but more symmetric in bias direction, and the TAMR ratio is comparatively larger due to better interface quality and lattice matching. When a QWRS forms close to the Fermi level at $t_{Fe} = 6$ MLs, we find a large QW-TAMR magnitude near zero bias [Fig. 3(e)]. On the other hand, when $t_{Fe} = 5$ MLs and the QWRS level is at 0.6 eV away from the Fermi level, the QW-TAMR magnitude decreases at zero bias, while QW-TAMR has a small magnitude at the QWRS level of -0.6 V. The quantization levels form either close to or far from zero bias depending on the parity of the number of Fe MLs, due to the Fe electronic structure [9,11,26]. The QW-TAMR magnitude correspondingly

shows oscillations in t_{Fe} with a two-ML period (Sec. S3 in the Supplemental Material [32]).

The origin of QW-TAMR in QW samples can be considered as follows. The M direction modifies the well potential via SOC and causes a shift or a modification of the majority-to-majority spin conduction channel in the QW transport. As an example, we see a main single-peak feature in the 6-ML sample at -3 mV in the in-plane magnetization direction, whereas a split spectrum is formed in the out-of-plane magnetization direction, with two fine-structure peaks at 11 and -57 mV [inset of Fig. 3(b)]. Hence a large anisotropy in G is observed. Similarly, at $t_{Fe} = 5$ MLs, there is an enhancement of TAMR at the QWRS of -600 mV. Other shifts in the fine peaks at $t_{Fe} = 5$ MLs are also found [inset of Fig. 3(c)]. In contrast, the TAMR effect in thick-Fe/(MgO, $MgAl_2O_4$)/thick-Fe is from the relatively small spin-flip transport channel dominated by the interfacial resonant states (IRSs) at an Fe surface [14,22]. The IRSs are shifted when magnetization is rotated, causing a change in spin-flip conductances [22,25,37]. This origin of thick-Fe TAMR is seen as a smoothing of G spectra in the inset of Fig. 3(a) upon the rotation of M. To sum up, the modulation of the dominant Δ_1 spin-conserved transport channel in an Fe-QW MTJ gives a larger QW-TAMR effect than the modulation of the much smaller IRS spin-flip transport channel of thick-electrode TAMR.

To further elucidate the main origin of QW-TAMR, we calculated the spin-dependent transport properties in the stack of Cr/Fe/MgO/Fe (001) by first-principles calculations, using the QUANTUM ESPRESSO package [38,39]. Figure 4(a) depicts the simulated structure of Al (5)/Cr (0 or 2)/Fe (1–8)/MgO (5)/Fe (5)/Al (2) (thicknesses in MLs), where the number of Fe MLs (n_{Fe}) was varied from 1 to 8. The density functional theory calculations are conducted with fully relativistic ultrasoft pseudopotentials and under the local-density approximation [40,41]. The number of k points was taken to be $20 \times 20 \times 1$ for electronic structure calculations and 100×100 for tunneling conductance calculations. Methfessel-Paxton smearing with a broadening parameter of 0.01 Ry was used. The cutoff energy for the wave function was set to 30 Ry, and that for the charge density was set to 300 Ry. The atomic positions are fully optimized in the calculations. The transmittance T is calculated with M oriented along either the Fe [001] or Fe [100] directions. The aluminium layers are included as an unpolarized bath of Δ_1 electrons. We confirmed the formation of the QWRSs by confinement between the two-ML Cr layer and the MgO barrier, while allowing for a nonvanishing conductance. The choice of MgO in the calculations is representative of the main effects in our QW. The tunneling transport is mainly through the oxygen sublattice [42]; the cation-disordered $MgAl_2O_4$ is equivalent to a lattice-matched MgO, and the band-folding effects can be ignored [43,44].

Figure 4(b) shows the dependence of the calculated TAMR on n_{Fe}, at the Fermi level. For the case without a Cr insertion (without QW), the TAMR is relatively small and shows a smooth dependence on n_{Fe}. On the other hand, in the formation of the QWRS by Cr insertion, QW-TAMR has a much larger magnitude and oscillates with n_{Fe}, similar to the experiments. We find the origin of the QW-TAMR to be the

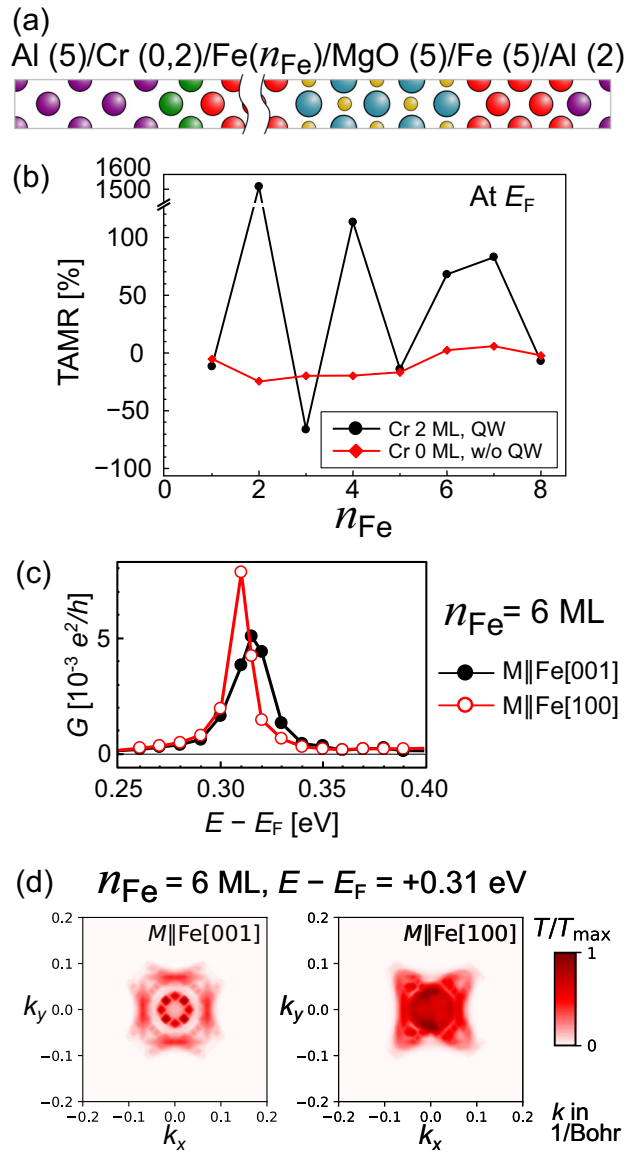

FIG. 4. Density functional theory calculations of QW-TAMR. (a) A depiction of the calculated structure. (b) The thickness dependence shows that TAMR oscillates with n_{Fe} for the QW case. (c) The energy dependence of average transmittance in Cr (two MLs)/Fe (six MLs)/MgO. The QWRS level has a shift induced by the rotation of M. (d) The calculated T-$k_{\|}$ map at resonance condition ($E_F + 0.31$ eV). The map is calculated for M oriented along the out-of-plane (left panel) and in-plane (right panel) directions. w/o, without.

anisotropic shift in QWRS. The interfacial magnetocrystalline anisotropy of the Fe/MgO interface changes the potential well leading to a shift in QWRS, and therefore QW-TAMR is observed. Figure 4(c) shows the energy dependence of the total conductance at $n_{Fe} = 6$ MLs. We find that the QWRSs are mainly formed by the Fe($d_{3z^2-r^2}$) states with the Δ_1 symmetry at the Fe/oxide and Cr/Fe interfaces. The Δ_1 QW states are confined by the potential of the interfacial bonding between Fe $d_{3z^2-r^2}$ and O p_z orbitals on one side, and the Fermi surface mismatch between Fe and Cr on the other side. The resonant tunneling through the QWRS is observed at $E = 0.315$ eV,

TABLE I. The spin-resolved conductance components of the QW calculated at $k_\parallel = (0, 0)$, $E = 0.315$ eV, where Fe thickness is six MLs. All the quantities are in units of conductance quantum e^2/h, where e and h are the electron charge and Planck's constant, respectively.

	$G_{\uparrow\uparrow}$	$G_{\uparrow\downarrow}$	$G_{\downarrow\uparrow}$	$G_{\downarrow\downarrow}$
$M\|\|$Fe [001]	0.6747	1.10×10^{-7}	1.10×10^{-7}	7.63×10^{-11}
$M\|\|$Fe [100]	0.4443	1.04×10^{-4}	1.04×10^{-4}	2.43×10^{-8}

where $E = 0$ eV corresponds to the Fermi level. The rotation of M causes a shift in the energy of the QWRS. The transmittance peak is shifted and increases in magnitude at $M\|\|$Fe [100] [Fig. 4(c)], which is consistent with the experiments. We note that the calculated QWRS energy positions do not match quantitatively with the experimental positions. This difference can be attributed to the different atomic configurations between the experiments and the calculations, especially at the Cr layer.

We analyze the components of conduction anisotropy in Table I, which lists the spin-conserved ($G_{\uparrow\uparrow}$, $G_{\downarrow\downarrow}$) and spin-flip ($G_{\uparrow\downarrow}$, $G_{\downarrow\uparrow}$) conductance components at $k_\parallel = (0, 0)$. The conduction is dominated by the resonant majority-to-majority spin tunneling in the present QW structure, and the spin-flip channel shows a very small magnitude. It is the modulation of the QWRS that causes the large anisotropy in the spin-conserved tunneling channel $G_{\uparrow\uparrow}$ and hence the large QW-TAMR effect. On the other hand, in the case of thick non-QW Fe electrodes, the spin-flip components through IRSs were the origin of the small non-QW TAMR effect [22,25,37].

The effect of M rotation on the QWRS can be understood further by looking into the $k_\parallel$-resolved transmittance map [Fig. 4(d)]. For $M\|\|$Fe [001], the T-$k_\parallel$ map is fourfold symmetric, with narrow resonant conduction peaks. When M lies along the Fe [100] direction, SOC causes a large deformation and broadening of the T-$k_\parallel$ map, and the rotational symmetry is broken. Mainly, the QW resonant transmittance at the Γ point is strongly modulated, while the IRSs at $k_\parallel \neq 0$ are also shifted, due to the change in the QW potential of Cr/Fe/MgO. In this case, T-$k_\parallel$ map of the $M\|\|$Fe [100] state loses the mirror symmetry around the k_y [010] axis. If the Rashba SOC is the origin of this QW-TAMR, the bands with $k \neq 0$ should divert along the k direction orthogonal to the magnetization [25,37] and therefore break the mirror symmetry around the k_x [100] axis. In our case, the asymmetry around the k_x axis in the T-$k_\parallel$ map is very small, indicating that the Rashba SOC contribution to the QW-TAMR is negligible. We note that the band-theory origin of bulk-Fe anisotropic magnetoresistance is related to the spin-flip scattering between Δ_2-symmetry states [25,45]. Hence a ballistic bulk-Fe anisotropic magnetoresistance (AMR) does not contribute to TAMR in MgO MTJs [25].

In summary, we observed a large QW-TAMR effect, where the rotation of QW magnetization modulates the majority-to-majority resonant transmission. We measured QW-TAMR in lattice-matched Cr/Fe/$MgAl_2O_4$ resonant tunnel junctions, in which the resonant states are symmetry selected for $\Delta_{1,\uparrow}$ electronic states. This QW-TAMR effect is present up to high temperatures, > 380 K. Analogous to semiconductor QW transistors, the magnetization angle has the same role as a transistor's gate voltage, where both can control the energy positions of quantization levels. We suggest that the magnetic gating of QWs by the spin degree of freedom can be applied to new electronic and optoelectronic devices, such as spin-polarized light sources and detectors [46].

The presented data and related supporting data are available from the authors upon reasonable request.

This work was partly supported by the ImPACT Program of the Council for Science, Technology and Innovation (Cabinet Office, Government of Japan) and JSPS KAKENHI Grant No. JP16H06332.

M.A.-M. is the corresponding author and conceived the project. M.A.-M., Q.X., and M.B. conducted the experiments, and Y.M. conducted the first-principles calculations. M.A.-M., Q.X., Y.M., M.B., K.M., S.K., H.S., and S.M. elaborated on the results and formulated the discussions. M.A.-M. wrote the manuscript with input from Y.M., S.M., H.S., and the other authors.

The authors declare no competing financial interests.

[1] L. Esaki and R. Tsu, IBM J. Res. Dev. **14**, 61 (1970).
[2] B. R. Nag, *Physics of Quantum Well Devices*, Solid-State Science and Technology Library (Springer, Amsterdam, 2000).
[3] K. Garrison, Y. Chang, and P. D. Johnson, Phys. Rev. Lett. **71**, 2801 (1993).
[4] N. V. Smith, N. B. Brookes, Y. Chang, and P. D. Johnson, Phys. Rev. B **49**, 332 (1994).
[5] R. K. Kawakami, E. Rotenberg, H. J. Choi, E. J. Escorcia-Aparicio, M. O. Bowen, J. H. Wolfe, E. Arenholz, Z. D. Zhang, N. V. Smith, and Z. Q. Qiu, Nature (London) **398**, 132 (1999).
[6] J. J. Paggel, T. Miller, and T.-C. Chiang, Science **283**, 1709 (1999).
[7] D.-A. Luh, J. J. Paggel, T. Miller, and T.-C. Chiang, Phys. Rev. Lett. **84**, 3410 (2000).
[8] T. Nozaki, N. Tezuka, and K. Inomata, Phys. Rev. Lett. **96**, 027208 (2006).
[9] T. Niizeki, N. Tezuka, and K. Inomata, Phys. Rev. Lett. **100**, 047207 (2008).
[10] B. S. Tao, H. X. Yang, Y. L. Zuo, X. Devaux, G. Lengaigne, M. Hehn, D. Lacour, S. Andrieu, M. Chshiev, T. Hauet, F. Montaigne, S. Mangin, X. F. Han, and Y. Lu, Phys. Rev. Lett. **115**, 157204 (2015).
[11] Q. Xiang, H. Sukegawa, M. Belmoubarik, M. Al-Mahdawi, T. Scheike, S. Kasai, Y. Miura, and S. Mitani, Adv. Sci. **6**, 1901438 (2019).
[12] S. Yuasa, T. Nagahama, A. Fukushima, Y. Suzuki, and K. Ando, Nat. Mater. **3**, 868 (2004).
[13] S. S. P. Parkin, C. Kaiser, A. Panchula, P. M. Rice, B. Hughes, M. Samant, and S.-H. Yang, Nat. Mater. **3**, 862 (2004).

[14] W. Butler, X.-G. Zhang, T. Schulthess, and J. MacLaren, Phys. Rev. B **63**, 054416 (2001).
[15] C. Gould, C. Rüster, T. Jungwirth, E. Girgis, G. M. Schott, R. Giraud, K. Brunner, G. Schmidt, and L. W. Molenkamp, Phys. Rev. Lett. **93**, 117203 (2004).
[16] Kirill I. Bolotin, F. Kuemmeth, and D. C. Ralph, Phys. Rev. Lett. **97**, 127202 (2006).
[17] L. Gao, X. Jiang, S.-H. Yang, J. D. Burton, E. Y. Tsymbal, and S. S. P. Parkin, Phys. Rev. Lett. **99**, 226602 (2007).
[18] J. Moser, A. Matos-Abiague, D. Schuh, W. Wegscheider, J. Fabian, and D. Weiss, Phys. Rev. Lett. **99**, 056601 (2007).
[19] R. S. Liu, L. Michalak, C. M. Canali, L. Samuelson, and H. Pettersson, Nano Lett. **8**, 848 (2008).
[20] B. G. Park, J. Wunderlich, D. A. Williams, S. J. Joo, K. Y. Jung, K. H. Shin, K. Olejník, A. B. Shick, and T. Jungwirth, Phys. Rev. Lett. **100**, 087204 (2008).
[21] B. G. Park, J. Wunderlich, X. Martí, V. Holý, Y. Kurosaki, M. Yamada, H. Yamamoto, A. Nishide, J. Hayakawa, H. Takahashi, A. B. Shick, and T. Jungwirth, Nat. Mater. **10**, 347 (2011).
[22] Y. Lu, H.-X. Yang, C. Tiusan, M. Hehn, M. Chshiev, A. Duluard, B. Kierren, G. Lengaigne, D. Lacour, C. Bellouard, and F. Montaigne, Phys. Rev. B **86**, 184420 (2012).
[23] K. Wang, T. L. A. Tran, P. Brinks, J. G. M. Sanderink, T. Bolhuis, W. G. van der Wiel, and M. P. de Jong, Phys. Rev. B **88**, 054407 (2013).
[24] I. Muneta, T. Kanaki, S. Ohya, and M. Tanaka, Nat. Commun. **8**, 15387 (2017).
[25] M. N. Khan, J. Henk, and P. Bruno, J. Phys.: Condens. Matter **20**, 155208 (2008).
[26] Z.-Y. Lu, X.-G. Zhang, and S. T. Pantelides, Phys. Rev. Lett. **94**, 207210 (2005).
[27] H. Sukegawa, H. Xiu, T. Ohkubo, T. Furubayashi, T. Niizeki, W. Wang, S. Kasai, S. Mitani, K. Inomata, and K. Hono, Appl. Phys. Lett. **96**, 212505 (2010).
[28] M. Belmoubarik, H. Sukegawa, T. Ohkubo, S. Mitani, and K. Hono, Appl. Phys. Lett. **108**, 132404 (2016).
[29] Q. Xiang, Z. Wen, H. Sukegawa, S. Kasai, T. Seki, T. Kubota, K. Takanashi, and S. Mitani, J. Phys. D: Appl. Phys. **50**, 40LT04 (2017).
[30] Q. Xiang, R. Mandal, H. Sukegawa, Y. K. Takahashi, and S. Mitani, Appl. Phys. Express **11**, 063008 (2018).
[31] S. Chikazumi, *Physics of Ferromagnetism* (Oxford University Press, Oxford, 2009), Chap. 12, pp. 260–262.
[32] See Supplemental Material at http://link.aps.org/supplemental/10.1103/PhysRevB.103.L180408, which includes Refs. [4,17,29,31,36,47,48], for the effects of magnetic anisotropy, the rotation plane, and the QW thickness on the angular dependence of QW-TAMR.
[33] I. B. Altfeder, K. A. Matveev, and D. M. Chen, Phys. Rev. Lett. **78**, 2815 (1997).
[34] J. P. Eisenstein, D. Syphers, L. N. Pfeiffer, and K. W. West, Solid State Commun. **143**, 365 (2007).
[35] A. Enders, T. L. Monchesky, K. Myrtle, R. Urban, B. Heinrich, J. Kirschner, X.-G. Zhang, and W. H. Butler, J. Appl. Phys. (Melville, NY) **89**, 7110 (2001).
[36] B. S. Tao, L. N. Jiang, W. J. Kong, W. Z. Chen, B. S. Yang, X. Wang, C. H. Wan, H. X. Wei, M. Hehn, D. Lacour, Y. Lu, and X. F. Han, Appl. Phys. Lett. **112**, 242404 (2018).
[37] A. N. Chantis, K. D. Belashchenko, E. Y. Tsymbal, and M. van Schilfgaarde, Phys. Rev. Lett. **98**, 046601 (2007).
[38] P. Giannozzi, S. Baroni, N. Bonini, M. Calandra, R. Car, C. Cavazzoni, D. Ceresoli, G. L. Chiarotti, M. Cococcioni, I. Dabo, A. D. Corso, S. de Gironcoli, S. Fabris, G. Fratesi, R. Gebauer, U. Gerstmann, C. Gougoussis, A. Kokalj, M. Lazzeri, L. Martin-Samos *et al.*, J. Phys.: Condens. Matter **21**, 395502 (2009).
[39] P. Giannozzi, O. Andreussi, T. Brumme, O. Bunau, M. B. Nardelli, M. Calandra, R. Car, C. Cavazzoni, D Ceresoli, M. Cococcioni, N. Colonna, I. Carnimeo, A. D. Corso, S. de Gironcoli, P. Delugas, R. A. DiStasio Jr., A. Ferretti, A. Floris, G. Fratesi, G. Fugallo *et al.*, J. Phys.: Condens. Matter **29**, 465901 (2017).
[40] H. J. Choi and J. Ihm, Phys. Rev. B **59**, 2267 (1999).
[41] A. Smogunov, A. Dal Corso, and E. Tosatti, Phys. Rev. B **70**, 045417 (2004).
[42] X.-G. Zhang, W. H. Butler, and A. Bandyopadhyay, Phys. Rev. B **68**, 092402 (2003).
[43] H. Sukegawa, Y. Miura, S. Muramoto, S. Mitani, T. Niizeki, T. Ohkubo, K. Abe, M. Shirai, K. Inomata, and K. Hono, Phys. Rev. B **86**, 184401 (2012).
[44] Y. Miura, S. Muramoto, K. Abe, and M. Shirai, Phys. Rev. B **86**, 024426 (2012).
[45] F. L. Zeng, Z. Y. Ren, Y. Li, J. Y. Zeng, M. W. Jia, J. Miao, A. Hoffmann, W. Zhang, Y. Z. Wu, and Z. Yuan, Phys. Rev. Lett. **125**, 097201 (2020).
[46] J. Yu, L. Wang, D. Yang, J. Zheng, Y. Xing, Z. Hao, Y. Luo, C. Sun, Y. Han, B. Xiong, J. Wang, and H. Li, Sci. Rep. **6**, 35597 (2016).
[47] C.-H. Lambert, A. Rajanikanth, T. Hauet, S. Mangin, E. E. Fullerton, and S. Andrieu, Appl. Phys. Lett. **102**, 122410 (2013).
[48] J. W. Koo, S. Mitani, T. T. Sasaki, H. Sukegawa, Z. C. Wen, T. Ohkubo, T. Niizeki, K. Inomata, and K. Hono, Appl. Phys. Lett. **103**, 192401 (2013).